


NANO EXPRESS

Open Access



MOF-Derived ZnSe/N-Doped Carbon Composites for Lithium-Ion Batteries with Enhanced Capacity and Cycling Life

Hongdong Liu^{1,2}, Zongyang Li³, Lei Zhang^{4*} , Haibo Ruan² and Rong Hu^{2*}

Abstract

In this work, three different morphologies of ZnSe/N-doped carbon (NC) composites are synthesized using ZIF-8 by a facile calcination process. By adjusting the particle size of precursor ZIF-8, the morphology and size of the product ZnSe/NC can be controlled. The as-prepared ZnSe/NC composites show excellent cyclic stability and rate capability as anode materials in lithium-ion batteries (LIBs). Especially, the as-obtained ZnSe/NC-300 exhibits reversible discharge capacity of 724.4 mAh g⁻¹ after 500 cycles at 1 A g⁻¹. The introduction of N-doped carbon can significantly improve the conductivity of ZnSe and promotes the transfer of electrons. And mesoporous structure is conducive to the penetration of electrolyte in active materials, increases the contact area, and alleviates the volume expansion during the charge-discharge process. Thus, ZnSe/NC composites provide a new insight into the development of anode materials for next-generation high-performance LIBs.

Keywords: Zinc selenide, N-doped carbon, MOFs, Lithium-ion batteries

Background

Lithium-ion batteries (LIBs) are widely used as a power source for portable electronic devices and vehicles owing to their high-energy density, long life, and environmental benignity [1–4]. However, present commercial graphite anode materials of LIBs have limited energy capacities and rate performance that are unable to meet the growing needs of high-energy-consuming fields. Lately, transition metal selenides (TMS) have been intensively investigated as anode materials for LIBs to substitute graphite due to their energy density and good cycling performance [5], such as SnSe [6], CoSe [7], Sb₂Se₃ [8], MoSe₂ [9], and FeSe [10]. Among these potential anode materials, zinc selenide (ZnSe) has attracted extensive interest owing to its high theoretical capacity, low cost, and unique electrochemical reaction mechanism [11]. However, ZnSe usually suffers from a large irreversible capacity and poor cycling stability due to a large volume expansion/contraction during Li-ion insertion and extraction process, which results in

electrode pulverization and loss of interparticle contact [12, 13]. To overcome these problems, designing nanostructures and combining various carbon materials to alleviate inevitable volume changes and increase conductivity have shown a good prospect for enhancing the electrochemical properties of metal selenides in LIBs. In particular, the N-doped carbon materials greatly change the electronic properties of carbon materials, provide more active sites, improve the interaction between lithium and carbon structure, and enhance the kinetic ability of lithium-ion diffusion and transfer. In addition, the introduction of heteroatoms results in a large number of lattice defects in carbon materials, which can form the disordered carbon structure and further improve lithium storage performance [14–18].

The multifunctional metal-organic frameworks (MOFs) possess many advantages, such as large specific surface area, high porosity, and various structures, and have shown great potential in a wide range of applications, including chemical sensors, gas adsorption/desorption, and catalytic application [19]. Recently, a variety of MOFs have been used as substrates, templates, or sacrificial precursors to fabricate multifunctional nanomaterials for LIBs [20–23]. Especially, TMS composites with carbonaceous

* Correspondence: leizhang0215@126.com; hurong_82@163.com

⁴College of Life Science, Chongqing Normal University, Chongqing 401331, People's Republic of China

²Research Institute for New Materials Technology, Chongqing University of Arts and Sciences, Chongqing 402160, People's Republic of China
Full list of author information is available at the end of the article

materials derived from MOFs not only accelerates Li-ion and electron transport, but also mitigates the large volumetric and structural variation during charge-discharge cycling, thus improving the electrochemical performance of LIBs [24, 25]. For example, Zhu et al. [14] reported ZnSe embedded in N-doped carbon nanocubes derived from ZIF-8 as anode materials for high-performance LIBs. The as-obtained ZnSe/carbon nanocomposite at 600 °C demonstrates a high initial discharge capacity of 1170.8 mAh g⁻¹ with the initial coulombic efficiency of 68.8% at the current density of 0.1 A g⁻¹. After 500 cycles, it still has high reversible capacity.

Herein, we utilized an important member of MOF family, ZIF-8, to synthesize three different morphologies of ZnSe/N-doped carbon (NC) composites by a facile calcination process. The resulting composites present excellent cyclic stability and rate capability as anode materials in LIBs. Particularly, the as-prepared ZnSe/NC-300 exhibits reversible discharge capacity of 724.4 mAh g⁻¹ after 500 cycles at 1 A g⁻¹. Hence, ZnSe/NC nanocomposites show outstanding electrochemical performance, which will be a potential high-performance anode material for LIBs.

Methods

Material Preparation

Synthesis of ZIF-8 Precursors

In a typical process, ZIF-8 was prepared by the commonly liquid phase method. Zn(NO₃)₂·6H₂O and 2-methylimidazole were used as raw materials and methanol was used as solvent. Firstly, 25 mmol of 2-methylimidazole and a certain amount of (0, 0.22, 0.44 mmol) Zn(NO₃)₂·6H₂O were dissolved in 250 ml methanol to form A solution and 12.5 mmol of Zn(NO₃)₂·6H₂O was dissolved in 250 ml methanol to obtain B solution. After the solution was completely dissolved, the solution B was poured into the solution A and exposed to ultrasound for 10 min. Subsequently, the mixed solutions were kept at room temperature for 24 h. After the reaction, the products were centrifugally washed many times with methanol and then dried in a vacuum drying chamber at 60 °C for 12 h. ZIF-8 with diameters of 900, 300, and 40 nm can be obtained, named ZIF-8-900, ZIF-8-300, and ZIF-8-40, respectively.

Synthesis of ZnSe/NC Composites

The as-prepared ZIF-8 was mixed with selenium powders according to the mass ratio of 1:1. The powders were mixed with a mortar and placed in a high-temperature tubular furnace. The ZnSe/NC composites were obtained 800 °C for 4 h under argon atmosphere. Both of the heating rate and cooling rate were 2 °C/min. The composites were named as ZnSe/NC-40, ZnSe/NC-300, and ZnSe/NC-900, respectively. In addition, the

commercial ZnSe was used as control group for comparative experiments.

Material Characterization

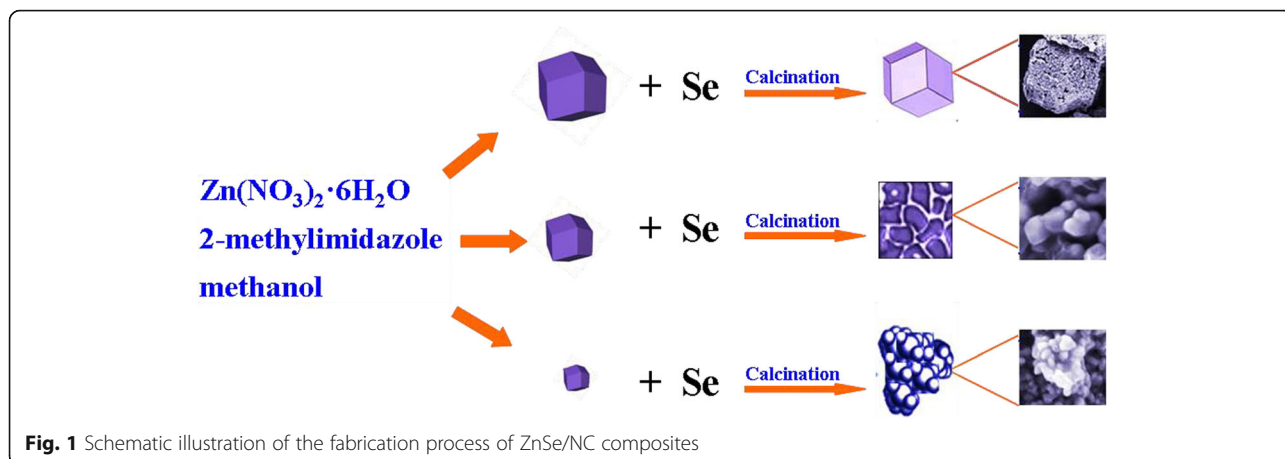
X-ray power diffraction (XRD) patterns were obtained from TD-3500 X-ray diffractometer equipped with Cu/Kα radiation ($\lambda = 0.15406$ nm) between 10° and 80° with a scanning rate of 4°min⁻¹. Raman spectra were employed with a micro-Raman spectrometer (LabRAM HR800) at a wavelength of 633 nm (1.96 eV). Specific surface area and pore size distribution were determined by a Belsorp II analyzer through the Brunauer-Emmett-Teller (BET) method and Barrett-Joyner-Halenda (BJH) model. The structure and morphology of ZnSe/NC were observed by field emission scanning electron microscope (FEI Quanta 250) and transmission electron microscopy (TEM-FEI Tecnai G2 F20). The main element composition of ZnSe/NC-300 was carried on X-ray photoelectron spectroscopy (XPS; Thermo VG ESCALAB 250XI).

Electrochemical Measurements

The electrochemical properties of ZnSe/NC composites and commercial ZnSe were investigated using coin-type cells (CR2032). Working electrodes were comprised of 80 wt.% active materials (ZnSe/NC-900, ZnSe/NC-300, ZnSe/NC-40, or commercial ZnSe), 10 wt.% acetylene black, and 10% wt.% polyvinylidene fluoride (PVDF). These materials were dispersed in *N*-methyl-2-pyrrolidone (NMP) to produce homogeneous slurry. Subsequently, the resultant slurry was coated uniformly onto a 10-μm-thick Cu foil using scraper technology and then dried in a vacuum oven for 8 h at 120 °C. A pure lithium sheet was used as counter electrode. The electrolyte was 1 M LiPF₆ (1.0 M) with the mixture of ethylene carbonate (EC) and dimethyl carbonate (DMC) (1:1 v/v). The polypropylene membrane (Celgard2400) served as the separator to electronically separate the two electrodes. The CR2032-type coin cells were assembled in an Ar-filled glove box. Galvanostatic cycling measurements were performed on a Neware battery test system (BTS-610) at various densities between 0.01 and 3.0 V. Cyclic voltammetry (CV) and electrochemical impedance spectroscopy (EIS) were carried out using a CHI760E electrochemical workstation. The scanning rate of CV was 0.2 mV/s at the range of 0.01–3.0 V, and the frequency range of EIS was between 0.1 Hz and 100 kHz.

Results and Discussion

Figure 1 illustrates the fabrication process of three different morphologies of ZnSe/NC composites by a facile chemical precipitation-calcination method. Firstly, the precursor ZIF-8 with different particle sizes are synthesized by dissolving different quantities of Zn(NO₃)₂·6H₂O and 2-methylimidazole in methanol for a period of time to

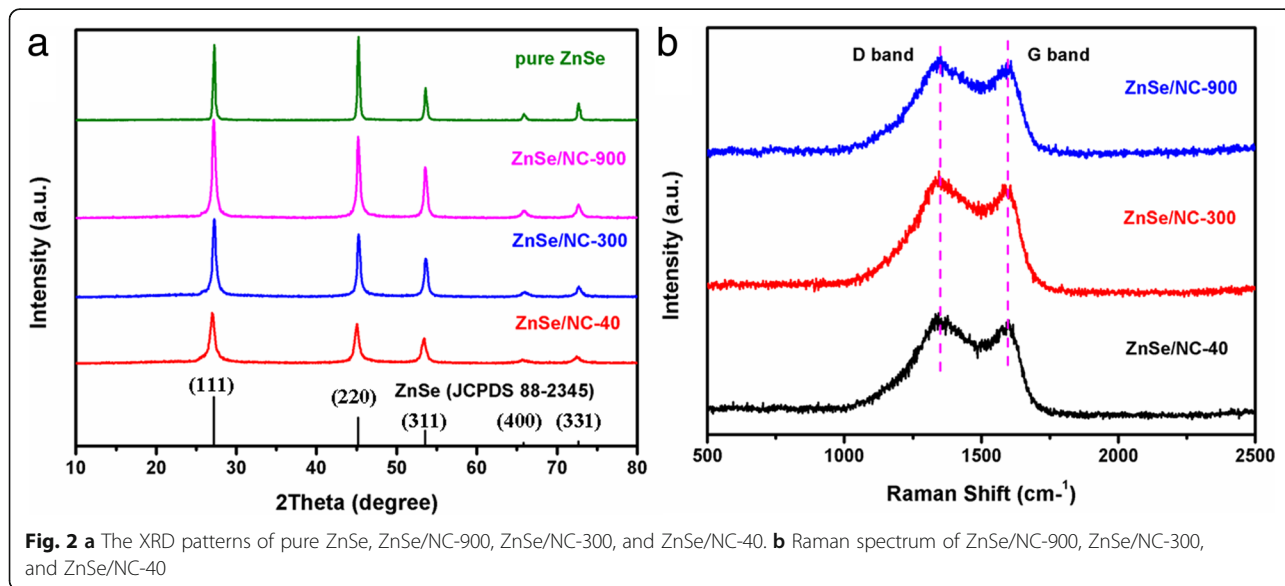


form precipitation. Among them, $\text{Zn}(\text{NO}_3)_2 \cdot 6\text{H}_2\text{O}$ provides zinc source, and 2-methylimidazole provides carbon source and nitrogen source. The crystallization of MOF(-ZIF-8) consists of two processes, nucleation and nucleation growth, which often proceed simultaneously and determine the crystal size together. Rapid nucleation is beneficial to the reduction of crystal size. Therefore, the crystal size of ZIF-8 can be significantly reduced by adding a small amount of metal ions in advance and then adding a large number of metal ions to make the nucleation grow up. Then, the as-prepared ZIF-8 and selenium powders are mixed in a certain proportion and calcined at high temperature in argon atmosphere to obtain ZnSe/NC composites. By adjusting the particle size of precursor ZIF-8, the morphology and size of the product ZnSe/NC can be controlled.

The XRD patterns of the samples are shown in Fig. 2a. The XRD spectra of pure ZnSe, ZnSe/NC-900, ZnSe/NC-

300, and ZnSe/NC-40 are consistent with the standard spectra of ZnSe (JCPDS 88-2345). The sharp diffraction peaks indicate that the as-prepared ZnSe/NC composites have high crystallinity. Moreover, the intensity of diffraction peaks of ZnSe/NC-40, ZnSe/NC-300, and ZnSe/NC-900 increase gradually, which indicates that the grain size of ZnSe phase increases, because ZnSe/NC inherits the grain size of precursor ZIF-8 to a certain extent. And no graphite-carbon bulges are found near $2\theta = 24^\circ$, which may be related to the lower content of C in ZnSe/NC composites and the existence form of C.

Raman spectra of ZnSe/NC-900, ZnSe/NC-300, and ZnSe/NC-40 were measured to investigate the existence of carbon and the form of carbon in ZnSe/C composites, respectively, as shown in Fig. 2b. Three samples of ZnSe/NC have a wide peak at about 1350 cm^{-1} and 1597 cm^{-1} , corresponding to the D-band and G-band vibrations of carbon, respectively. D peak is usually considered to be



caused by disordered vibration of defects in carbon materials, while G peak is caused by in-plane stretching vibration of carbon atoms with sp^2 , which is the characteristic peak of graphite carbon [26]. The existence of D and G peaks indicates that carbon exists in ZnSe/NC, which is formed by carbonization of organic ligand 2-methylimidazole in ZIF-8 at high temperature. The ID/IG values of ZnSe/NC-900, ZnSe/NC-300, and ZnSe/NC-40 are 1.03, 1.04, and 1.02, respectively. The ID/IG values of the three composites are relatively close and large, which indicates that the graphitization degree of carbon in ZnSe/NC composites is low and there are many defects. According to the relevant literature [27], defects in carbon materials can be used as residual lithium storage reaction of active sites to increase capacity.

The morphologies of ZnSe/NC-900, ZnSe/NC-300, and ZnSe/NC-40 were measured by FESEM, as shown in Fig. 3a–c. The rhombic dodecahedron morphology of ZnSe/NC-900 can be observed in Fig. 3a; the inset shows the SEM image of precursor ZIF-8. And the dodecahedron is composed of numerous ZnSe nanoparticles of about 100 nm in size, and the outer layer of the whole dodecahedron is coated with a thin carbon layer. However, ZnSe/NC-300 cannot maintain the dodecahedron morphology, but shows nanoparticles with a particle size of about 20–50 nm, and ZnSe is encapsulated by carbon

layers. ZnSe/NC-40 is also a nanoparticle with a particle size of about 10–20 nm and carbon layers wrapped in the outer layer, but its agglomeration is serious. Figure 3d shows the BET curve of ZnSe/NC-300. It can be observed that the nitrogen adsorption and desorption curve of ZnSe/NC-300 composites have obvious hysteresis loops in the range of relative pressure 0.5–0.9 p/p_0 , indicating that they are type IV isothermal curves. At the same time, the hysteresis loop is H3 type, which indicates the existence of mesoporous structure in ZnSe/NC composites. According to Brunauer-Emmett-Teller (BET) theory, the specific surface area of ZnSe/C-300 is $93.926 \text{ m}^2 \text{ g}^{-1}$. The inset of Fig. 3d is a pore diameter distribution curve based on Barrett-Joyner-Halenda (BJH) theory. The average pore size of ZnSe/NC-300 is 4.4095 nm, which is typical mesoporous structure. According to the relevant literature [28], mesoporous structure is conducive to the penetration of electrolyte in the active materials, increases the contact area between the electrolyte and the active materials, enlarges the reactive sites, and promotes the diffusion of lithium ions. Furthermore, mesoporous structure can also alleviate the volume expansion and stress during charge-discharge process and improves cycle stability.

The morphology and crystal structure of ZnSe/NC-300 were further characterized by TEM. ZnSe/NC-300 cannot inherit the rhombohedral dodecahedron morphology of

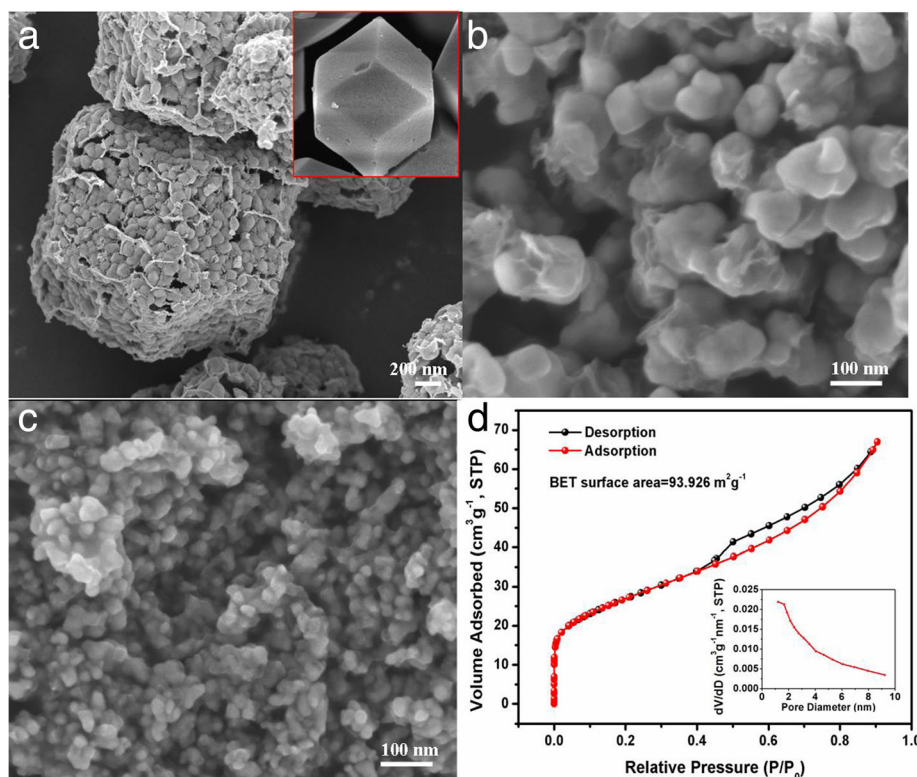


Fig. 3 a–c SEM images of ZnSe/NC-900, ZnSe/NC-300, and ZnSe/NC-40, respectively, inset of SEM image of ZIF-8. **d** Nitrogen adsorption-desorption isotherms of ZnSe/NC-300, inset of pore diameter distribution profiles of ZnSe/NC-300

the precursor ZIF-8, but shows nano-granular architecture with particle size of about 20–50 nm in Fig. 4a, b. Figure 4c is a HRTEM image of ZnSe/NC composites, from which uniform carbon layers and lattice fringes can be clearly seen. The crystal plane spacing in ZnSe/NC-300 is 0.33 nm, corresponding to (111) crystal plane of ZnSe. This result is consistent with the XRD and XPS. Figure 4d is the selected area electron diffraction pattern of ZnSe/NC-300. It can be seen that the patterns of electron diffraction are all diffraction rings, not uniform diffraction spots. It shows that the as-prepared ZnSe/NC-300 composites are polycrystalline.

XPS spectra of ZnSe/C-300 composites were measured for further analysis of the element composition and the existing state of each element. The characteristic peaks of Zn (Zn 2p), Se (Se 3s, Se 3P and Se 3d), C (C 1s), N (N 1s), and O (O 1s) can be seen from the full spectrum of XPS (Additional file 1: Figure S3), which indicates that Zn, Se, C, N, and O are five elements in ZnSe/C-300. N may be derived from organic ligand 2-methylimidazole, which is carbonized to form N-doped carbon during high-temperature calcination. The O 1s peak can be associated

with the adsorbed O₂, CO₂, and H₂O in the air or the surface oxidation of the samples [14]. Figure 5 a–d are Zn 2p, Se 3d, C 1s, and N 1s high-resolution XPS spectra of ZnSe/NC-300, respectively. From Fig. 5a, it can be seen that there are two characteristic peaks at 1044.65 eV and 1021.62 eV in the spectrum of Zn 2p, corresponding to Zn 2p_{1/2} and Zn 2p_{3/2} in ZnSe, respectively, and the difference of binding energy value between the two peaks is $\Delta E = 23.03$ eV, which indicates that Zn in the ZnSe/NC-300 mainly exists in the form of Zn⁺². Three characteristic peaks can be seen from the high-resolution spectra of Fig. 5b Se 3d. The peaks at 54.7 eV and 53.82 eV correspond to Se 3d_{3/2} and Se 3d_{5/2}, while the broad peak at 59.09 eV corresponds to Se-O; it may be that the exposure of ZnSe/NC-300 to air results in the oxidation of the surface layer to SeO_x. Figure 5c is a high-resolution C 1s spectrum of ZnSe/NC-300, from which three characteristic peaks at 284.7 eV, 285.49 eV, and 287.48 eV can be seen, corresponding to sp²C, N-sp²C, and N-sp³C, respectively. In Fig. 5d N 1s, there are three characteristic peaks located at 400.74 eV, 399.26 eV, and 398.47 eV, corresponding to graphite nitrogen, pyrrolidine nitrogen, and pyridine

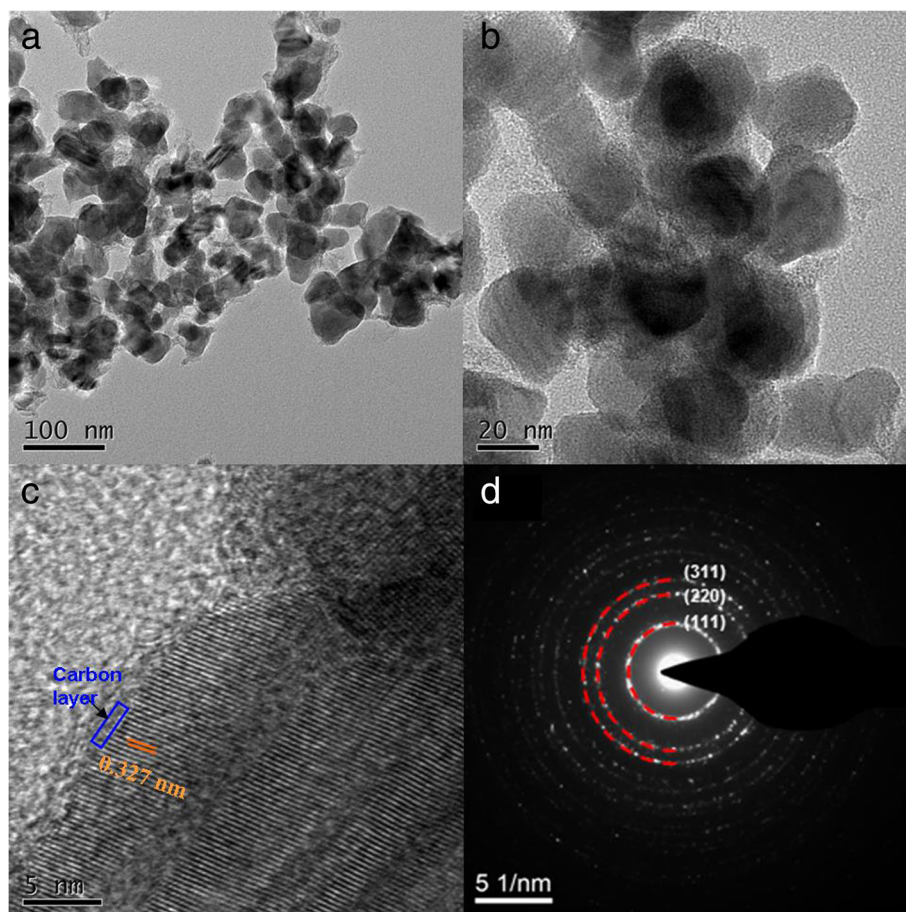
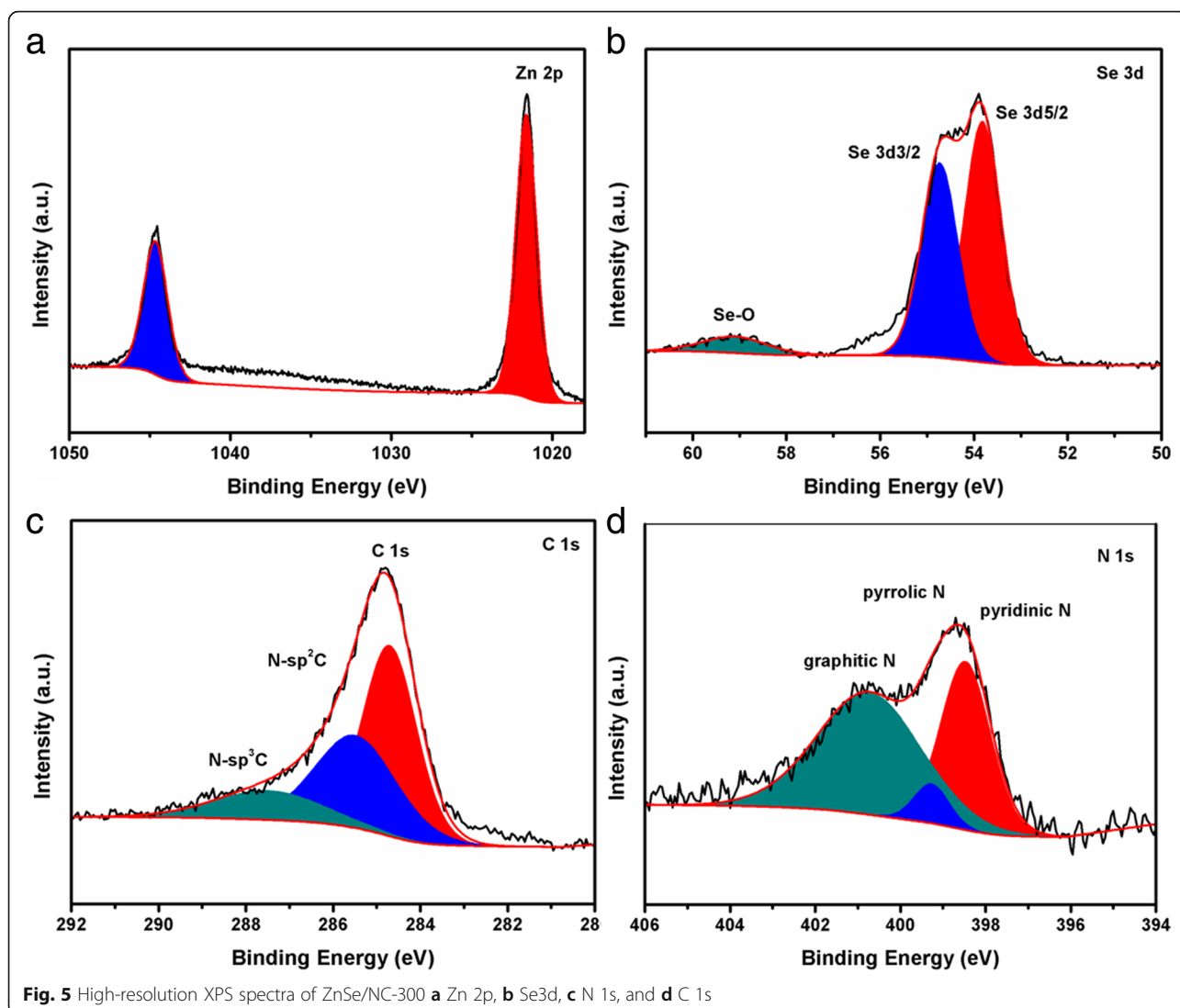


Fig. 4 a, b TEM images of ZnSe/NC-300. c HRTEM image of ZnSe/NC-300. d SAED image of ZnSe/NC-300



nitrogen, respectively. According to the relevant literature [29], pyrrolidine and pyridine nitrogen can be used as active sites to participate in lithium storage reaction and improve the capacity of materials. In addition, N doping can provide enough electrons for the π conjugate system and further improves its conductivity [30–33]. Therefore, it can be seen that ZnSe/NC-300 is composed of ZnSe and N-doped carbon, which is consistent with the results of XRD and Raman.

In order to investigate the lithium storage mechanism of ZnSe/NC composites, the CV curves of ZnSe/NC-300 composites were measured. As shown in Fig. 6a, there is a weak reduction peak at 1.5 V and a sharp reduction peak at 0.35 V in the first discharge process of ZnSe/NC composites. According to previous reports [11, 29], the reduction peak at 1.5 V is caused by the formation of SEI film on the surface of active materials. The reduction peak at 0.35 V indicates that lithium ion is embedded in the crystal

structure of ZnSe, ZnSe is reduced to form Zn and Li_2Se , and Zn and Li-ion are alloyed to form Li_xZn alloy phase. In the first charging process, there are several small oxidation peaks below 1.0 V, which correspond to the multi-step de-alloying reaction of Li_xZn alloy phase. The sharp oxidation peak at about 1.4 V corresponds to the formation of ZnSe by oxidation of Zn. In addition, several oxidation peaks can be observed at about 2.5 V for ZnSe/NC composites, which may be related to the oxidation of Li_2Se to Se. In the following two cycles, the reduction and oxidation peaks of ZnSe/NC composites deviate from those of the first cycle, which may be caused by the restructuring of ZnSe/NC composites during charging and discharging.

Figure 6b shows the galvanostatic charge-discharge curve of ZnSe/NC-300 measured at the current density of 100 mA g^{-1} and voltage window of 0.01–3.0 V. It can be seen that there is a discharge platform at about 0.75 V in the first discharge process of ZnSe/NC composites.

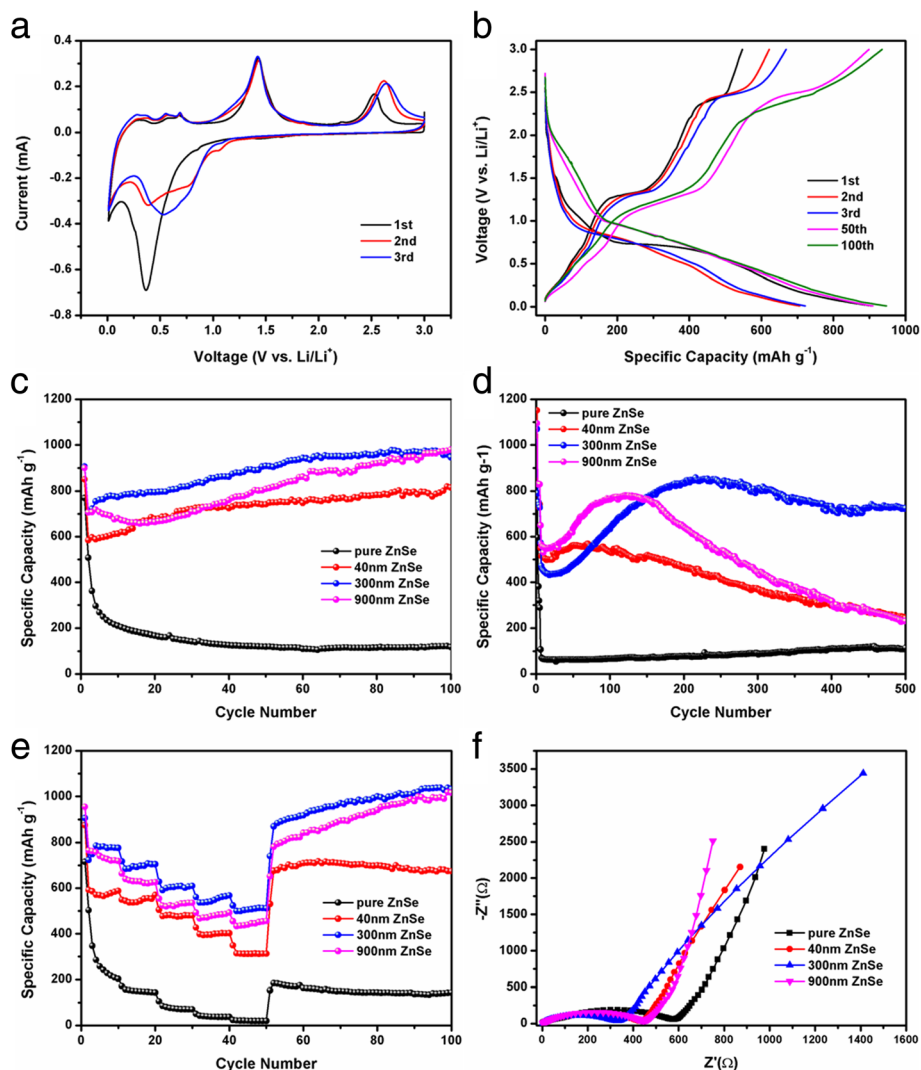


Fig. 6 **a** The first three cyclic CV curves of ZnSe/NC-300. **b** Galvanostatic charge-discharge curves at the current density of 100 mA g^{-1} . **c** The cycling performance of pure ZnSe, ZnSe/NC-900, ZnSe/NC-300, and ZnSe/NC-40 at the current density of 100 mA g^{-1} . **d** The cycling performance of pure ZnSe, ZnSe/NC-900, ZnSe/NC-300, and ZnSe/NC-40 at the current density of 1 A g^{-1} . **e** Rate performance of pure ZnSe, ZnSe/NC-900, ZnSe/NC-300, and ZnSe/NC-40 at the current densities ranging from 0.1 to 2 A g^{-1} . **f** EIS spectra of pure ZnSe, ZnSe/NC-900, ZnSe/NC-300, and ZnSe/NC-40 before cycling

During the first charging process, there is a charging platform around 1.3 V. They correspond to the insertion and removal of lithium ions, respectively. During the subsequent charge-discharge process, the discharge platform changes from 0.75 to 0.9 V, while the charge platform does not change significantly. The results are in good agreement with those of CV curves.

The first charge-discharge capacities of ZnSe/NC-300 are $547.48 \text{ mAh g}^{-1}$ and $906.66 \text{ mAh g}^{-1}$, respectively. The initial coulomb efficiency is 60.3%. The lower coulomb efficiency and irreversible capacity in the first cycle are caused by the irreversible decomposition of electrolytes on the surface of active materials to form SEI films. Moreover, the charge-discharge curves of the 50th and

100th cycles are also shown in Fig. 6b. It can be found that the discharge capacities of the 50th and 100th cycles of ZnSe/NC composites increase significantly compared with the first three cycles, which may be caused by the pseudo-capacitance behavior.

Cycle performances of ZnSe/NC composites were further investigated at the current densities of 100 mA g^{-1} . It can be seen from Fig. 6c that the discharge capacity of ZnSe/NC composites shows an increasing trend. After 100 cycles, the discharge capacity of ZnSe/NC-900 increases from $705.85 \text{ mAh g}^{-1}$ in the second cycle to $979.15 \text{ mAh g}^{-1}$. The corresponding capacity of ZnSe/NC-300 increases from 706.05 to $947.11 \text{ mAh g}^{-1}$. The capacity of ZnSe/NC-40 rises from 584.58 to 814.6 mAh g^{-1} .

According to the previous literature [14], this capacity growth phenomenon is caused by the pseudo-capacitance behavior. The pseudo-capacitance is due to the formation of a highly reversible gel polymer layer on the surface of the active materials. This reaction includes the oxidation-reduction reaction on the surface and near the surface of active materials and the rapid insertion of particles. The capacity growth phenomenon caused by pseudo-capacitance is common in transition metal compounds which store lithium through conversion reaction.

In addition, the discharge capacity of ZnSe/NC composites is much higher than that of pure ZnSe in the whole cyclic testing process. This is because that the introduction of N-doped carbon can significantly improve the conductivity of ZnSe and promotes the transfer of electrons. At the same time, pyrrole-N and pyridine-N can be used as reactive sites to participate in lithium storage reaction and improve lithium storage capacity. Furthermore, mesoporous structure is conducive to the penetration of electrolyte in active materials, increases the contact area, and alleviates the volume expansion during the charge-discharge process.

Figure 6d shows the cyclic behavior of ZnSe/NC composites at a high current density of 1 A g^{-1} . The first five cycles are carried out at a current density of 100 mA g^{-1} . The purpose is to generate a dense SEI film on the surface of the active materials for the subsequent cycling performance test at the high current density of 1 A g^{-1} . The discharge capacity of ZnSe/NC composites shows a trend of first increasing and then decreasing. The discharge capacity of ZnSe/NC-300 increases to $858.05 \text{ mAh g}^{-1}$ in the 216th cycle and decreases to 724.4 mAh g^{-1} in the 500th cycle. It is significantly superior than that of the previous literatures (Additional file 1: Table S1). The discharge capacity of ZnSe/NC-900 rises to $779.86 \text{ mAh g}^{-1}$ in the 121st cycle and reduces to $229.54 \text{ mAh g}^{-1}$ in the 500th cycle. The capacity of ZnSe/NC-40 improves to the maximum at the 70th cycle and drops to $243.27 \text{ mAh g}^{-1}$ at the 500th cycle.

Figure 6e shows the rate performance curves of pure ZnSe, ZnSe/NC-900, ZnSe/NC-300, and ZnSe/NC-40 (0.1–2 A). After 10 cycles at the current densities of 100 mA g^{-1} , 200 mA g^{-1} , 500 mA g^{-1} , 1 A g^{-1} , and 2 A g^{-1} , respectively, the corresponding discharge capacities of ZnSe/NC-300 are $775.65 \text{ mAh g}^{-1}$, $704.14 \text{ mAh g}^{-1}$, $609.26 \text{ mAh g}^{-1}$, $567.68 \text{ mAh g}^{-1}$, and $511.59 \text{ mAh g}^{-1}$. The corresponding discharge capacities of ZnSe/NC-900 are $718.59 \text{ mAh g}^{-1}$, $625.73 \text{ mAh g}^{-1}$, $534.94 \text{ mAh g}^{-1}$, $492.61 \text{ mAh g}^{-1}$, and $455.28 \text{ mAh g}^{-1}$, respectively. The discharge capacities of ZnSe/NC-40 are $587.73 \text{ mAh g}^{-1}$, $569.35 \text{ mAh g}^{-1}$, $479.64 \text{ mAh g}^{-1}$, $402.31 \text{ mAh g}^{-1}$, and $312.57 \text{ mAh g}^{-1}$, respectively. In addition, as the current density decreases to 100 mA g^{-1} , the discharge capacity of ZnSe/NC-40 remains basically stable, while the

discharge capacity of ZnSe/NC-300 and ZnSe/NC-900 shows an increasing trend. When the current density drops to 100 mA g^{-1} , the discharge capacity of ZnSe/NC-300 recovers to $739.89 \text{ mAh g}^{-1}$, and increases to $1031.66 \text{ mAh g}^{-1}$ after 50 cycles. The discharge capacity of ZnSe/NC-900 is restored to $651.97 \text{ mAh g}^{-1}$, and raised to $1016.07 \text{ mAh g}^{-1}$ after 50 cycles. The above results show that the structure of ZnSe/NC composites has not been damaged obviously after the rate performance test, and the integrity of the structure has been maintained, presenting a good rate performance. Compared with ZnSe/NC-300 and ZnSe/NC-900, the rate performance of ZnSe/NC-40 is worse. This may be due to its smaller specific surface area (Additional file 1: Figure S4), which reduces the contact area between ZnSe/NC and electrolyte, and is not conducive to the diffusion of lithium ions.

The impedance of the material has a significant effect on its electrochemical properties. Figure 6f shows the AC impedance spectra of pure ZnSe and ZnSe/NC composites before cyclic testing. It can be seen that the AC impedance spectra consist of a half circle in the high-frequency region and an oblique line in the low-frequency region. The diameter of the semicircle represents the charge transfer resistance, while the slope of the oblique line presents the Warburg impedance, which is related to the diffusion of lithium ions in the electrode materials. The semicircle diameter of ZnSe/NC composite is obviously smaller than that of pure ZnSe, which indicates that the charge transfer impedance of ZnSe/NC decreases because the introduction of N-doped carbon promotes the electron transfer and reduces the resistance. The AC impedance spectroscopy (Additional file 1: Figure S7) of ZnSe/C composites after 100 cycles shows that the semicircle diameter of the composites at high frequency decreases significantly, which may be related to the activation behavior during the cyclic process.

Conclusions

In summary, three different morphologies of ZnSe/NC composites have been synthesized by using ZIF-8 nanocubic templates followed by a facile calcination method. By adjusting the particle size of precursor ZIF-8, the morphology of the product ZnSe/NC can be controlled. As a result, ZnSe/NC composites exhibit excellent cyclic stability and rate capability as anode materials in LIBs. Particularly, the as-obtained ZnSe/NC-300 presents that the first discharge and charge capacity are 906.66 and $547.48 \text{ mAh g}^{-1}$ at the current density of 100 mA g^{-1} , respectively. After 500 cycles, the reversible discharge capacity is still maintained at 724.4 mAh g^{-1} at 1 A g^{-1} . The introduction of N-doped carbon can significantly improve the conductivity of ZnSe and promotes the transfer of electrons. And the large specific surface area

and mesoporous structure are conducive to the penetration of electrolyte in active materials, increase the contact area, and alleviate the volume expansion during the charge-discharge process. Therefore, the as-prepared ZnSe/NC nanocomposites show superior electrochemical performance, which will be a potential high-performance anode material for LIBs.

Additional file

Additional file 1: Figure S1. SEM images of ZIF-8 at different sizes (a) ZIF-900, (b) ZIF-300, (c) ZIF-40, and (d) the XRD patterns of synthesized ZIF-8 at different sizes and simulated XRD pattern. **Figure S2.** (a, b) TEM images of ZnSe/NC-900 and ZnSe/NC-40, respectively, (c, d) HRTEM images of ZnSe/NC-900 and ZnSe/NC-40, respectively, (e, f) SAED images of ZnSe/NC-900 and ZnSe/NC-40, respectively. **Figure S3.** XPS survey spectra of ZnSe/NC-300. **Figure S4.** (a, b) Nitrogen adsorption-desorption isotherms of ZnSe/NC-900 and ZnSe/NC-40, respectively, (c, d) their pore diameter distribution profiles. **Figure S5.** The first three cyclic CV curves of (a) pure ZnSe, (b) ZnSe/NC-900, and (c) ZnSe/NC-40 at a scan rate of 0.2 mV/s in the range of 0.01–3.0 V. **Figure S6.** Galvanostatic discharge/charge voltage profiles of (a) pure ZnSe, (b) ZnSe/NC-900, (c) ZnSe/NC-40 at a current density of 100 mA g⁻¹. **Figure S7.** EIS spectra of pure ZnSe, ZnSe/NC-900, ZnSe/NC-300, and ZnSe/NC-40 after 100 cycles. **Table S1.** Comparison of ZnSe/NC composites and other metal selenides as LIB anodes. (DOC 2425 kb)

Abbreviations

LIBs: Lithium-ion batteries; NC: N-doped carbon; TMS: Transition metal selenides; MOFs: Metal-organic frameworks; XRD: X-ray power diffraction; BET: Brunauer-Emmett-Teller; BJH: Barrett-Joyner-Halenda; TEM: Transmission electron microscopy; PVDF: Polyvinylidene fluoride; EC: Ethylene carbonate; DMC: Dimethyl carbonate; CV: Cyclic voltammetry; EIS: Electrochemical impedance spectroscopy

Acknowledgements

Special thanks to Professor Jiamu Huang of Chongqing University for the useful comments.

Authors' Contributions

HL and ZL synthesized and characterized the samples. ZL and RH analyzed the data. HL and LZ designed the experiments and wrote the paper. All authors read and approved the final manuscript.

Funding

This work is supported by the Technology and Basic and Frontier Research Program of Chongqing Municipality (cstc2018jcyjAX0701 and cstc2017jcyjAX0326), Major Program of Chongqing University of Arts and Sciences (P2017XC06), and the Open Project Fund of Chongqing University New Energy Storage Devices and Application Engineering Research Center (KF20170105).

Availability of Data and Materials

All data are fully available without restriction.

Competing Interests

The authors declare that they have no competing interests.

Author details

¹Engineering Research Center of New Energy Storage Devices and Applications, Chongqing University of Arts and Sciences, Chongqing 402160, People's Republic of China. ²Research Institute for New Materials Technology, Chongqing University of Arts and Sciences, Chongqing 402160, People's Republic of China. ³College of Materials Science and Engineering, Chongqing University, Chongqing 400045, People's Republic of China. ⁴College of Life Science, Chongqing Normal University, Chongqing 401331, People's Republic of China.

Received: 27 April 2019 Accepted: 19 June 2019

Published online: 15 July 2019

References

- Zhang C, Jin C, Teng G, Gu Y, Ma W (2019) Controllable synthesis of hollow MnFe₂O₄ by self-etching and its application in high-performance anode for lithium-ion batteries. *Chem Eng J* 365:121–131
- Liu H, Huang J, Li X, Liu J, Zhang Y, Du K (2012) Flower-like SnO₂/graphene composite for high-capacity lithium storage. *Appl Surf Sci* 258:4917–4921
- Wang W, Li J, Bi M, Zhao Y, Chen M, Fang Z (2018) Dual function flower-like CoP/C nanosheets: high stability lithium-ion anode and excellent hydrogen evolution reaction catalyst. *Electrochimica Acta* 259:822–829
- Zhao Y, Wang W, Chen M, Wang R, Fang Z (2018) The synthesis of ZnS@MoS₂ hollow polyhedrons for enhanced lithium storage performance. *Crystengcomm* 20:7266–7274
- Lu T, Dong S, Zhang C, Zhang L, Cui G (2017) Fabrication of transition metal selenides and their applications in energy storage. *Coord Chem Rev* 332:75–99
- Yoon YH, Kim DS, Kim M, Park MS, Lee YC, Kim KH, Kim IT, Hur J, Lee SG (2018) Investigation of electrochemical performance on carbon supported tin-selenium bimetallic anodes in lithium-ion batteries. *Electrochimica Acta* 266:193–201
- Chen T, Li S, Wen J, Gui P, Fang G (2017) Metal-organic framework template derived porous CoSe₂ nanosheet arrays for energy conversion and storage. *ACS Appl Mat Interfaces* 9:35927–35935
- Luo W, Gaumet JJ, Magri P, Diliberto S, Li F, Franchetti P, Ghanbaja J, Mai L (2019) Fast green microwave-assisted synthesis of single crystalline Sb₂Se₃ nanowires towards promising lithium storage. *J Energy Chem* 30:27–33
- Wu L, Tan P, Liu Y, Shang Y, Liu W, Xiong X, Pan J (2017) In situ formation of carbon encapsulated nanosheet-assembled MoSe₂ hollow nanospheres with boosting lithium storage. *J Colloid Interf Sci* 491:279–285
- Wei D, Liang J, Zhu Y, Hu L, Zhang K, Zhang J, Yuan Z, Qian Y (2014) Layer structured alpha-FeSe: a potential anode material for lithium storage. *Electrochem Commun* 38:124–127
- Ma D, Zhu Q, Li X, Gao H, Wang X, Kang X, Tian Y (2019) Unraveling the impact of ether and carbonate electrolytes on the solid-electrolyte interface and the electrochemical performances of ZnSe@C core-shell composites as anodes of lithium-ion batteries. *ACS Appl Mat Interf* 11:8009–8017
- Kwon H-T, Park C-M (2014) Electrochemical characteristics of ZnSe and its nanostructured composite for rechargeable Li-ion batteries. *J Power Sources* 251:319–324
- Fu Y, Zhang Z, Du R, Qu Y, Li Q, Yang X (2015) Spherical-like ZnSe with facile synthesis as a potential electrode material for lithium ion batteries. *Mat Lett* 146:96–98
- Zhu L, Wang Z, Wang L, Xie L, Li J, Cao X (2019) ZnSe embedded in N-doped carbon nanocubes as anode materials for high performance Li-ion batteries. *Chem Eng J* 364:503–513
- Zhang D, Li G, Li B, Fan J, Liu X, Chen D, Li L (2019) A facile strategy to fabricate V₂O₅/porous N-doped carbon nanosheet framework as high-performance anode for lithium-ion batteries. *J Alloys Compounds* 789:288–294
- Yang Z, Wang J, Wu HT, Kong FJ, Yin WY, Cheng HJ, Tang XY, Qian B, Tao S, Yi J, Ma YS, Yuan RX (2019) MOFs derived Co_{1-x}S nanoparticles embedded in N-doped carbon nanosheets with improved electrochemical performance for lithium ion batteries. *Appl Surface Sci* 479:693–699
- Xue H, Yue S, Wang J, Zhao Y, Li Q, Yin M, Wang S, Feng C, Wu Q, Li H, Shi D, Jiao Q (2019) MoS₂ microsphere@ N-doped carbon composites as high performance anode materials for lithium-ion batteries. *J Electroanal Chem* 840:230–236
- Xu X, Niu F, Wang C, Li Y, Zhao C, Yang J, Qian Y (2019) Li₃VO₄ nanoparticles in N-doped carbon with porous structure as an advanced anode material for lithium-ion batteries. *Chem Eng J* 370:606–613
- Falcao P, Ricco R, Yazdi A, Imaz I, Furukawa S, Maspoch D, Ameloot R, Evans JD, Doonan CJ (2016) Application of metal and metal oxide nanoparticles@MOFs. *Coord Chem Rev* 307:237–254
- Zheng G, Chen M, Zhang H, Zhang J, Liang X, Qi M, Yin J (2019) Zn-MOFs derived porous carbon nanofiber for high performance lithium-ion batteries. *Surf Coat Technol* 359:384–389
- Shao M, Cheng Y, Zhang T, Li S, Zhang W, Zheng B, Wu J, Xiong W-W, Huo F, Lu J (2018) Designing MOFs-derived FeS₂@carbon composites for high-rate sodium ion storage with capacitive contributions. *ACS Appl Mat Interf* 10:33097–33104

22. Zeng P, Li J, Ye M, Zhuo K, Fang Z (2017) In situ formation of $\text{Co}_9\text{S}_9/\text{N-C}$ hollow nanospheres by pyrolysis and sulfurization of ZIF-67 for high-performance lithium-ion batteries. *Chem Eur J* 23:9517–9524
23. Zhao Y, Bi M, Qian F, Zeng P, Chen M, Wang R, Liu Y, Ding Y, Fang Z (2018) Heterostructure $\text{CoS}/\text{NC}@/\text{MoS}_2$ hollow spheres for high-performance hydrogen evolution reactions and lithium-ion batteries. *Chemelectrochem* 5:3953–3960
24. Wang X, Wang L, Chen B, Yao J, Zeng H (2016) MOFs as reactant: in situ synthesis of $\text{Li}_2\text{ZnTi}_3\text{O}_8/\text{C-N}$ nanocomposites as high performance anodes for lithium-ion batteries. *J Electroanal Chem* 775:311–319
25. Chen Y, Wu J, Yang W, Fu Y, Zhou R, Chen S, Zhang L, Song Y, Wang L (2016) Zn/Fe-MOFs-derived hierarchical ball-in-ball $\text{ZnO}/\text{ZnFe}_2\text{O}_4/\text{carbon}$ nanospheres with exceptional lithium storage performance. *J Alloys Compd* 688:211–218
26. Liu H, Hu Z, Su Y, Ruan H, Hu R, Zhang L (2017) MnO_2 nanorods/3D-rGO composite as high performance anode materials for Li-ion batteries. *Appl Surface Sci* 392:777–784
27. Zhang M, Jia M (2013) High rate capability and long cycle stability Fe_3O_4 -graphene nanocomposite as anode material for lithium ion batteries. *J Alloys Compounds* 551:53–60
28. Liu H, Huang J, Li X, Liu J, Zhang Y (2013) Green synthesis of SnO_2 nanosheets and their electrochemical properties. *Ceram Int* 39:3413–3415
29. Chen Z, Wu R, Wang H, Zhang KHL, Song Y, Wu F, Fang F, Sun D (2018) Embedding ZnSe nanodots in nitrogen-doped hollow carbon architectures for superior lithium storage. *Nano Res* 11:966–978
30. Wang Y, Li Y, Mao SS, Ye D, Liu W, Guo R, Feng Z, Kong J, Xie J (2019) N-doped porous hard-carbon derived from recycled separators for efficient lithium-ion and sodium-ion batteries. *Sustain Energy Fuels* 3:717–722
31. Zhang D, Wang G, Xu L, Lian J, Bao J, Zhao Y, Qiu J, Li H (2018) Defect-rich N-doped porous carbon derived from soybean for high rate lithium-ion batteries. *Appl Surface Sci* 451:298–305
32. Wang N, Liu Q, Sun B, Gu J, Yu B, Zhang W, Zhang D (2018) N-doped catalytic graphitized hard carbon for high-performance lithium/sodium-ion batteries. *Scientific Reports* 8:1–8
33. Alkarmo W, Ouhib F, Aqil A, Thomassin J-M, Vertruyen B, Piedboeuf M-L, Job N, Detrembleur C, Jerome C (2018) Continuous-porous N-doped carbon network as high-performance electrode for lithium-ion batteries. *J Mat Sci* 53:6135–6146

Publisher's Note

Springer Nature remains neutral with regard to jurisdictional claims in published maps and institutional affiliations.

Submit your manuscript to a SpringerOpen[®] journal and benefit from:

- Convenient online submission
- Rigorous peer review
- Open access: articles freely available online
- High visibility within the field
- Retaining the copyright to your article

Submit your next manuscript at ► [springeropen.com](https://www.springeropen.com)
